Article

Not peer-reviewed version

Transferable, Transparent and Flexible Pseudocapacitors from Ternary V2O5/PEDOT/Graphene Electrodes with High Durability in Organic Electrolyte

Sanju Gupta * and Brendan Evans

Posted Date: 10 January 2023

doi: 10.20944/preprints202301.0172.v1

Keywords: Solid-state supercapacitors, flexibility, transferability, energy storage, SECM

Article

Transferable, Transparent and Flexible Pseudocapacitors from Ternary V_2O_5/PEDOT/Graphene Electrodes with High Durability in Organic Electrolyte

Sanju Gupta [1,2,*] and Brendan Evans [2,†]

[1] Department of Materials Science and Engineering, Pennsylvania State University, University Park, PA 16802, USA
[2] Department of Physics and Astronomy and Advanced Materials Institute, Western Kentucky University, Bowling Green, KY 42101, USA
* Correspondence: sgup77@gmail.com
† The co-author (B.E.) was an undergraduate student participant.

Abstract: Transparent conductive electrodes (TCEs) are of enormous significance to the emergence of flexible and wearable electronics and continued growth of modern devices. Versatile and tunable TCEs, featuring with not only high optical transmittance but also intriguing features of electrochemical energy-storage capability, remain a significant challenge. Here we develop capacitive active films comprised of graphene-conjugated V_2O_5@poly (3,4-ethylene dioxythiophene) ternary composite (V_2O_5@PEDOT/rGO) on silver nanowire coated substrates as solid-state super/pseudocapacitors. The constructed electrodes exhibit improved electrolyte ions interaction with effective graphene layer, achieving high areal capacitance 0.6-1.2 mF.cm^{-2} with 0.5M LiCl electrolytes at optical transparency >60% with record durability. As demonstrated, the kinetic blocking of PEDOT layer and anchoring capability of graphene upon amphoteric soluble vanadium ions from layered V_2O_5 nanoribbons/nanobelts contribute synergistically to the unusual electrochemical stability, also shown using scanning electrochemical microscopy (SECM) providing electroactivity sites and ion transportation rates. As-fabricated symmetric solid-state supercapacitors delivered broad potential window >1.4 V under two different electrolyte environments (aqueous LiCl and LiCl/PVA gel) and demonstrated higher power and energy density (0.27 μWh.cm^{-2}) outperforming previously reported devices at <0.1 μWh.cm^{-2}. The electrochemical properties are also discussed in terms of solvation in polymer gel electrolyte ions.

Keywords: solid-state supercapacitors; flexibility; transferability; energy storage; SECM

Introduction

Intense demand of electric power on global scale calls for developing alternative and sustainable energy sources. Electrochemical energy conversion and storage (EECS) systems represent the most environmentally benign technologies capable to deliver higher power density with moderate energy density and longer cycle life in contrast to intermittent solar and wind energy. Intense research activity in EECS, namely rechargeable secondary batteries and electrochemical super- and pseudo-capacitors is motivated by the need for next generation of stable, cost-effective high-performing electrode materials and architectures. While supercapacitors store energy by forming a double layer of electrolyte ions on the surface of electrodes, the conversion is between electricity and energy stored in chemical bonds (pseudocapacitive or faradaic redox reactions). However, it is noteworthy that in practical supercapacitor electrodes, the two energy storage mechanisms abovementioned often work concomitantly.

 doi:10.20944/preprints202301.0172.v1

A great deal of interest in developing solid-state capacitors (SSCs), offering flexibility for wearable electronics, is recognized as potentially safe systems for future energy conversion, storage and harvesting. Their development involves solid-state electrolytes which contain polymer gel and ion liquid electrolytes [1–3]. In addition, transparent conductive electrodes (TCEs) with higher optical transparency are equally promising for emerging modern electronic and photonic devices such as tactile screens, photovoltaics, interactive portable electronics, and liquid crystal displays [4–6]. Regarding the development of transparent solid-state supercapacitors, not only high transparency, and high conductivity but also efficient electrochemical performance is highly indispensable. To realize high-performance transparent supercapacitors, one would achieve a high figure of merit determined evaluating optoelectronic and electrochemical properties *i.e.,* by the ratio of DC to optical conductivity (σ_{DC}/σ_{OP}), via developing metallic TCEs with a higher transmittance and lower sheet resistance [7–11]. To this end, metallic networks have been fabricated and integrated with inherently non-transparent capacitive materials [7,12], As a result, capacitive materials with intrinsic transparent nature such as CNTs [13], graphene [14–16], conductive polymers [4,17,18], and MXenes [19] have been of particular interest for transparent supercapacitors in recent years. However, the energy density was below 0.1 $\mu Wh.cm^{-2}$, due to the limited capacitive materials in metallic networks, or low capacitance and narrow voltage window. Besides, transparent films transferable to various substrates can make them suitable and cater to electronics manufacturing [20]. Therefore, pursuing capacitive materials with intrinsic transparent nature, good energy-storage capability, and even transferability for constructing high-performance transparent supercapacitors is crucial.

Nanotechnology accelerated the innovations in electrode formulations and architectures to replace conventional carbon-based materials as supercapacitive and transition metal oxides and polymers as pseudocapacitive cathodes [21,22]. Among nanocarbons, two-dimensional graphene based functional nanomaterials (GFNs) show enormous potential for electrochemical applications and the designer interfaces with other nanomaterials further alleviate issue of quantum capacitance by increasing density of states near Fermi level in addition to tunable physical-chemical properties (specific surface area, mechanical strength, facile electron and ion transportation, higher electron mobility and conductivity) [23–28]. Among known pseudocapacitive materials offering high energy density, nanoscale or nanostructured vanadium pentoxide (V_2O_5) and conducting polymers (CPs) have been broadly investigated. Due to layered structure of V_2O_5 and layered polymers, they are capable to intercalate three Li^+ ions per unit arising from its multivalent oxidation states and wide operating potential window [29–33]. Nevertheless, they suffer from severe capacity degradation arising from the formation of soluble vanadium-based ions (*e.g.*, V^{3+}, VO^+ , VO^{2+}, $H_2VO_4^-$, and $HV_2O_5^-$) [34,35]. However, researchers have pioneered several advances to enhance cycling stability of V_2O_5 by hybridizing with graphene and/or CPs such as polypyrrole (PPy) and polyaniline (PANI) [17,24,25,36,37]. The low electronic conductivity of V_2O_5 necessitates combining with conducting graphene materials [38,39]. Moreover, a comprehensive understanding of the underlying mechanism, and further enhancement in cyclic durability for reliable energy-storage devices is lacking.

Two-dimensional graphene having higher specific surface area, higher electrical conductivity, and mechanical strength offers a strategic choice to interface with V_2O_5 and PEDOT (poly 3,4-Ethylenedioxythiophene) polymer forming ternary hybrid electrodes as high-performing cathodes. In this regard, we proposed to prepare quasi graphene *i.e.,* reduced graphene oxide (rGO) conjugated V_2O_5@PEDOT (denoted as V_2O_5@PEDOT/rGO) ternary hybrid advanced formulations for constructing transparent capacitive electrode material on flexible plastic substrates. The results are compared with those of individual constituents for comparison in LiCl-based aqueous and organic electrolytes, the latter to investigate as solid-state supercapacitors. The unique hybrids showed excellent transparency and flexibility and is transferable to various substrates while maintaining structural integrity. The electrode made of the hybrids and silver nanowire (AgNW) networks shows higher areal capacitance (0.8 $mF.cm^{-2}$) at the optical transparency of > 60%. More importantly, the resulting electrode exhibits a record electrochemical stability over 100 000 cycles, benefitting from the blocking effect of the conformally PEDOT layer (insulating layer) and the chemisorption of rGO

 doi:10.20944/preprints202301.0172.v1

toward soluble vanadium-based ions, as unveiled experimentally and corroborated theoretically. The as-assembled symmetric solid-state transparent supercapacitor of V_2O_5@PEDOT/rGO hybrid delivers a high energy density of 0.25–0.36 μWh.cm^{-2}, superior to those similar transparent supercapacitors existed in the literature. Meanwhile utilizing advanced electrochemical microscopy, we obtained insights into the physicochemical processes occurring at the electrode-electrolyte interfaces and imaged electroactivity. Finally, a prototype unit of the assembled device with organic electrolyte is shown to light up commercial light-emitting diode (LED) bulb. The intrinsic capacitive charge-storage capability and easy transferability holds great promise for practical applications in the fields of high-performing transparent solid-state supercapacitors (SSCs).

Experimental

Materials and Methods

Chemical synthesis of V_2O_5@PEDOT nanobelts and electrodes assembly of V_2O_5@PEDOT/rGO. 3 g of commercial V_2O_5 powder (Sigma-Aldrich) was added into 100 mL NaCl aqueous solution (2 mol. L^{-1}), and then 1.5 mL of EDOT (3,4-Ethylenedioxythiophene) monomer was added dropwise. The mixture was stirred continuously for 5 days (120h) at a rate of 650 rpm.min^{-1}. The dark green solution was washed three times by deionized (DI) water and ethanol through centrifugation, respectively. Finally, the V_2O_5@PEDOT nanobelts were obtained by dispersing the above obtained product in DI water and ultrasonication for 2h. The control samples of vanadium pentoxide (V_2O_5) nanoribbons/nanobelts were prepared by the same method without using EDOT monomer.

Firstly, reduced graphene oxide (rGO) was prepared chemically according to the previous work. Briefly, 4.2 mL of GO suspension (15 mg. mL^{-1}) was dispersed in 300 mL of DI water and sonicated for 2h at room temperature. Subsequently, 60 μL of hydrazine and 1mL of ammonia (25%) were added into the GO suspension and stirred for 1h at 90 °C. The graphene suspension was obtained by dialyzing for 2-2.5 days. To prepare V_2O_5@PEDOT/rGO, 125 mL of V_2O_5@PEDOT (0.1 mg. mL^{-1}) suspension was injected into 50 mL of graphene suspension (0.125 mg. mL^{-1}) in 30 min. to form a homogeneous suspension. The optimal mass ratio between V_2O_5@PEDOT and reduced graphene oxide (rGO) was 2.5:1.

Transfer process of V_2O_5@PEDOT/rGO films. The V_2O_5@PEDOT/rGO films were obtained by filtration with different amounts of V_2O_5@PEDOT/rGO suspension, in which a cellulose acetate (CA) membrane with the pore size of 0.22 μm was used. Once the filtration is finished, the membrane was placed on target substrates in inverted position with a pressure of 10 MPa. After peeling off the membrane, the V_2O_5@PEDOT/rGO films were successfully transferred onto the PET (5 cm × 5 cm) and other substrates.

Preparation of Ag networks. Long silver nanowires (AgNW) were prepared according to the reported method [40]. The prepared Ag nanowires (30-50 nm diameter) with lengths up to 50-55 μm were dispersed into ethanol, forming a uniform suspension (0.25 mg. mL^{-1}). The Ag networks on PET were fabricated by spin coating. The PET film was pre-treated by plasma for 2 min. The spin coating was conducted by dropping 500 μL Ag suspension on PET with rotation speed 500 rpm.min^{-1} for 10s, followed by 2000 rpm.min^{-1} for 45s. This process was repeated for 10-15 times. After spin-coating, the obtained film was further treated by argon plasma for 5 min.

Preparation of transparent electrodes and devices. The transparent electrodes with different thicknesses were prepared by transferring the V_2O_5@PEDOT/rGO films onto the AgNW networks via the same method afore mentioned. The mass loading of transparent electrodes with thickness of 31 nm is measured to be about 57 μg.cm^{-2} and the area of electrodes is 2 cm^2. As for the control, samples of V_2O_5 nanobelts/nanoribbons and V_2O_5@PEDOT for various tests, the spin coating was used to prepare electrodes and control the mass loading of active materials same as V_2O_5@PEDOT/rGO electrodes. The gel electrolyte of LiCl/PVA was prepared following the reported work [41,42]. To assemble the symmetric supercapacitor, two transparent electrodes coated with the electrolyte were sandwiched face-to-face. After placing in ambient surrounding for one day to be dried, solid-state supercapacitor (SSCs) is constructed with area of 1.2 cm^2 approximately. Allowing more

Preprints (www.preprints.org) | NOT PEER-REVIEWED | Posted: 10 January 2023 doi:10.20944/preprints202301.0172.v1

understanding the interaction between rGO and V_2O_5@PEDOT, we measured room temperature electrical (I-V) properties' in-plane configuration. We made electrical contacts with colloidal silver paste and attached a Cu wire for connection with the Keithley 2400 source meter (Keithley, Cleveland, OH, USA). We measured two-point contact resistance and determined room temperature electrical conductivity (σ_{dc}) for all the samples studied.

Materials Characterization

Electron microscopy, crystal structure, and lattice vibrational measurements. All the samples were characterized for surface morphology, crystal structure and electrochemical properties. Scanning electron microscopy (SEM) images were taken using field-emission SEM with an instrument (Model JEOL 5400LV, MA) operating at primary electron acceleration voltage (V_{acc}) of 10 kV and at constant current 45 μA in secondary electron imaging mode collected with an in-lens detector. X-ray diffraction (XRD) patterns obtained with Siemens Model D5000 instrument (Thermo Scientific, MA) in Bragg-Brentano θ-2θ geometry ranging 2θ from 8° to 60° using Cu K_α X–ray source (λ =1.5405 Å) operating at voltage 45 kV and current 40 mA. Samples were run at a scan rate of 0.04 °/s or to improve signal-to-noise ratio, we also measured at scan rate 0.02°/s. The approximate BET surface area of the composites is 675 $m^2\ g^{-1}$. Raman spectra were measured to determine chemical bonding phases measured using a micro-Raman spectrometer (Model InVia Renishaw *plc*, Hoffman Estates, IL, USA) equipped with a laser providing excitation wavelength 633 nm (E_L=1.92 eV). The scattered light is collected in backscattering geometry transmitted and detected by CCD camera. An objective lens of 50x was used providing a spot size of ~1–2 μm and the laser power on the sample is maintained between < 0.1–0.5 mW (1% or 5%) to avoid local heating effects preventing photo-thermal degradation. The Raman spectra were acquired from 60–180s depending upon the laser power used and to maximize throughput signal. Raman spectra ranged from 120–3200 cm^{-1} samples with spectral resolution of 1 cm^{-1}. Transmittance spectra were investigated by Lambda 35 in the wavelength between 300 and 800 nm and air were set as blank sample to evaluate the transmittance of PET (polyethylene terephthalate) and related electrode samples. All the electrochemical tests examined using an electrochemical workstation (Model 920D CHI, TX). Electrochemical properties included cyclic voltammetry (CV), electrochemical impedance spectroscopy (EIS) and galvanostatic charging discharging (GCD) cyclability. The thickness of samples was determined by atomic force microscope with a scratch.

Electrochemical measurements. Electrochemical properties of the transparent electrodes evaluated in a custom designed three-electrode system, in which a Pt plate, Ag/AgCl electrode and 0.5M LiCl aqueous solution and 0.5M LiCl in water soluble polyvinyl alcohol (PVA) used as the counter electrode, reference electrode and (aqueous and organic) electrolytes, respectively. The electrochemical performance of solid-state pseudo/supercapacitors was studied by CV and GCD tests conducted in the potential range between −0.8V and +0.8V at scan rates between 5 mV/s and 500 mV/s and in the voltage range from 0V to 1.4V. GCD tests were conducted using cathode and anode currents ranging from 1 mA to 1A (or $1mA.g^{-1}$ to $1A.g^{-1}$). Each test allowed the cell to charge for 20 seconds or until its voltage reached 1V at which point the cell began discharging and this cycle repeated several times. We also measured two-point electrical properties (I-V) to determine room temperature dc electrical conductivity (σ). Areal capacitance (C_a) analogous to the gravimetric specific capacitance (C_g) of transparent electrodes and symmetric devices based on CV curves and GCD curves are calculated following:

$$C_a = \frac{1}{\Delta V \times v \times A} I(V)dV \quad (1)$$

$$C_a = \frac{I \times \Delta t}{\Delta V \times A} I(V)dV \quad (2)$$

Or

Preprints (www.preprints.org) | NOT PEER-REVIEWED | Posted: 10 January 2023 doi:10.20944/preprints202301.0172.v1

$$C_g = \frac{I \times \Delta t}{\Delta V \times m} I(V)dV \quad (2')$$

where I (A), ΔV (V), v ($V.s^{-1}$), A (cm^2), and Δt (s) are current, potential window, scan rate, the geometrical area immersed in the electrolyte and discharge time after IR drop, respectively. The areal energy density (E) and power density (P) of the devices calculated according to the following equations:

$$P = \frac{(\Delta V \times I)}{A} = \frac{3600\,E}{\Delta t} \quad (3)$$

$$E = \frac{(\mathrm{P} \times \Delta t)}{3600} = \frac{1}{2}\frac{1}{3600} C_a \Delta V^2 \quad (4)$$

in which P, is the power density ($\mu W.cm^{-2}$), E the energy density ($\mu Wh.cm^{-2}$), C_a ($mF.cm^{-2}$) are the real capacitance calculated from GCD curves, ΔV(V) is the operating potential window calculated as ΔV = $|V_{max}–V_{min}|$ / 2, P, is the power density ($\mu W.cm^{-2}$), and $\Delta t\,(s)$ is the discharge time. Scanning electrochemical microscopy (SECM) was performed to gain insights into electrode/electrolyte interface and to capture electroactivity in aqueous and organic electrolytes with 5mM $K_3Fe(CN)_6$ (potassium ferricyanide) as redox mediator. Measurements included CV in microelectrode configuration between -0.9 – +0.6V at scan rate v = 20 mV/s, probe approach with tip voltage V_t = +0.4V and substrate voltage Vs = -0.5V (polarity 1; Pol1) and Vs = +0.5V (polarity 2; Pol2), and SECM imaging with these polarities in probe area 400 μm × 400 μm with 2 μm increment [17,43,44].

Results and Discussion

Microscopic Structure and Morphology

Figure 1 shows the fabrication of the V_2O_5@PEDOT/rGO hybrids via multi-step liquid phase deposition method. Firstly, V_2O_5 nanobelts/nanoribbons are formed chemically followed by core-shell structured V_2O_5@PEDOT nanobelts were synthesized via recrystallization and concurrent coating process using commercial V_2O_5 powders as raw materials. Subsequently, in virtue of the strong π–π conjugations between PEDOT and reduced graphene oxide (rGO), the V_2O_5@PEDOT hybrid and rGO nanosheets are assembled simultaneously. Through filtration and peeling, self-supported transparent hybrid films of V_2O_5@PEDOT/rGO could be achieved, which is easily transferred onto any other substrates such as PET coated with and without silver nanowires (AgNW) for current conduction [45]. Scanning electron microscopy (SEM) and X-ray diffraction (XRD) demonstrate the morphological and crystallographic evolution of V_2O_5 from powders to nanobelts/nanoribbons (40-70 nm) in the presence of EDOT polymeric molecules. Thinner V_2O_5 nanobelts in sodium-containing solutions are formed through dissolution and recrystallization process [46]. Figure 2a,b presents representative SEM and TEM images along with SAED patterns of as-prepared prepared constituents, supported rGO and freestanding graphene paper post filtration, crystalline V_2O_5 nanobelts and their conjugation with PEDOT and rGO nanosheets. Corresponding XRD pattern and Raman spectra are shown in Figures 2c and 2d, respectively.

Preprints (www.preprints.org) | NOT PEER-REVIEWED | Posted: 10 January 2023 doi:10.20944/preprints202301.0172.v1

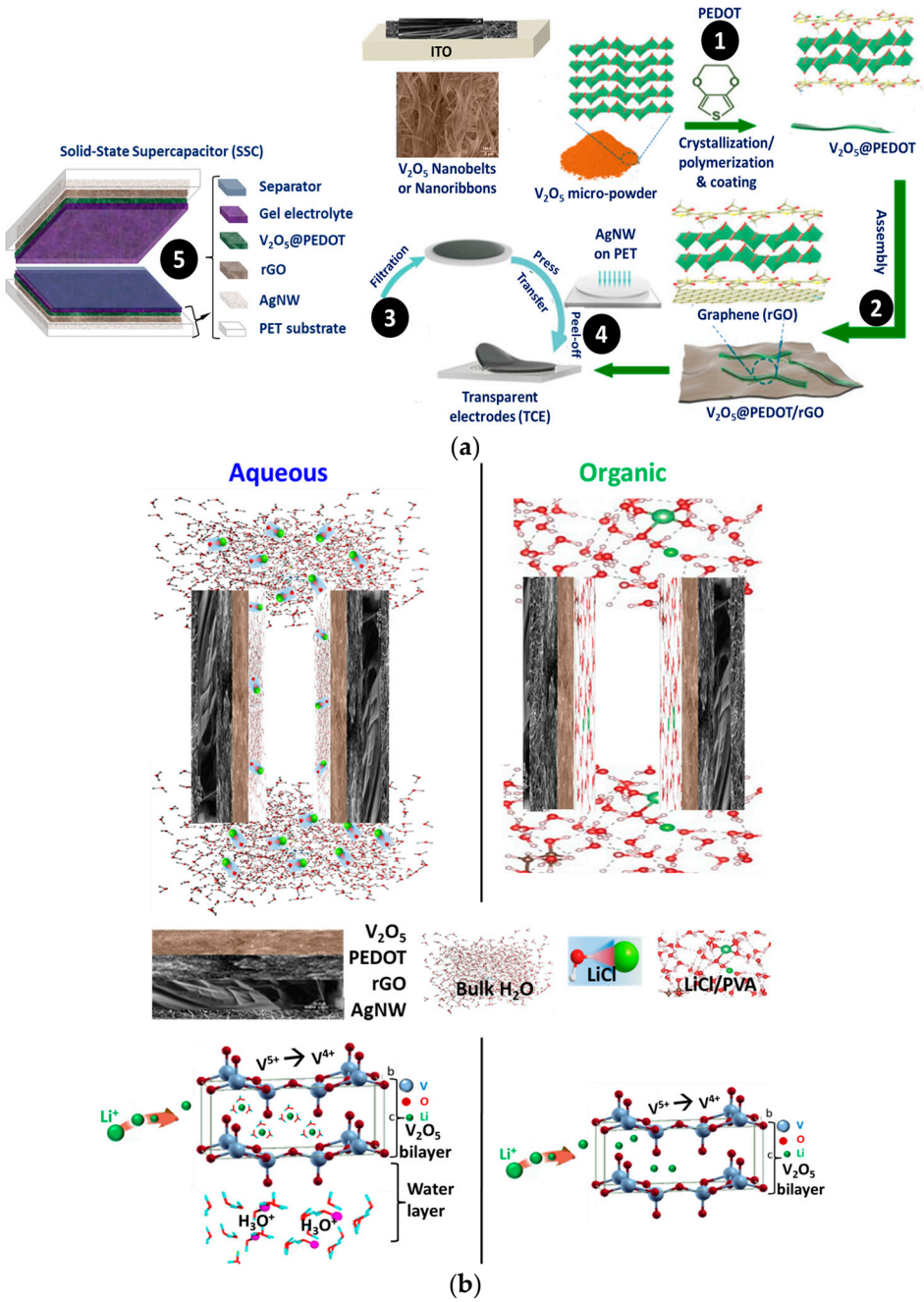

Figure 1. | (a) Schematic flow of synthesis for preparing and transferring graphene based 'hybrid' supercapacitor electrodes (V_2O_5@PEDOT/rGO) on conducting and flexible PET substrates and an assembly of solid-state supercapacitor (SSC) and with components for half-cell. (b) Configurations for electrolyte structure and solvation dynamics in aqueous and organic electrolyte. (Gupta et al.).

Preprints (www.preprints.org) | NOT PEER-REVIEWED | Posted: 10 January 2023 doi:10.20944/preprints202301.0172.v1

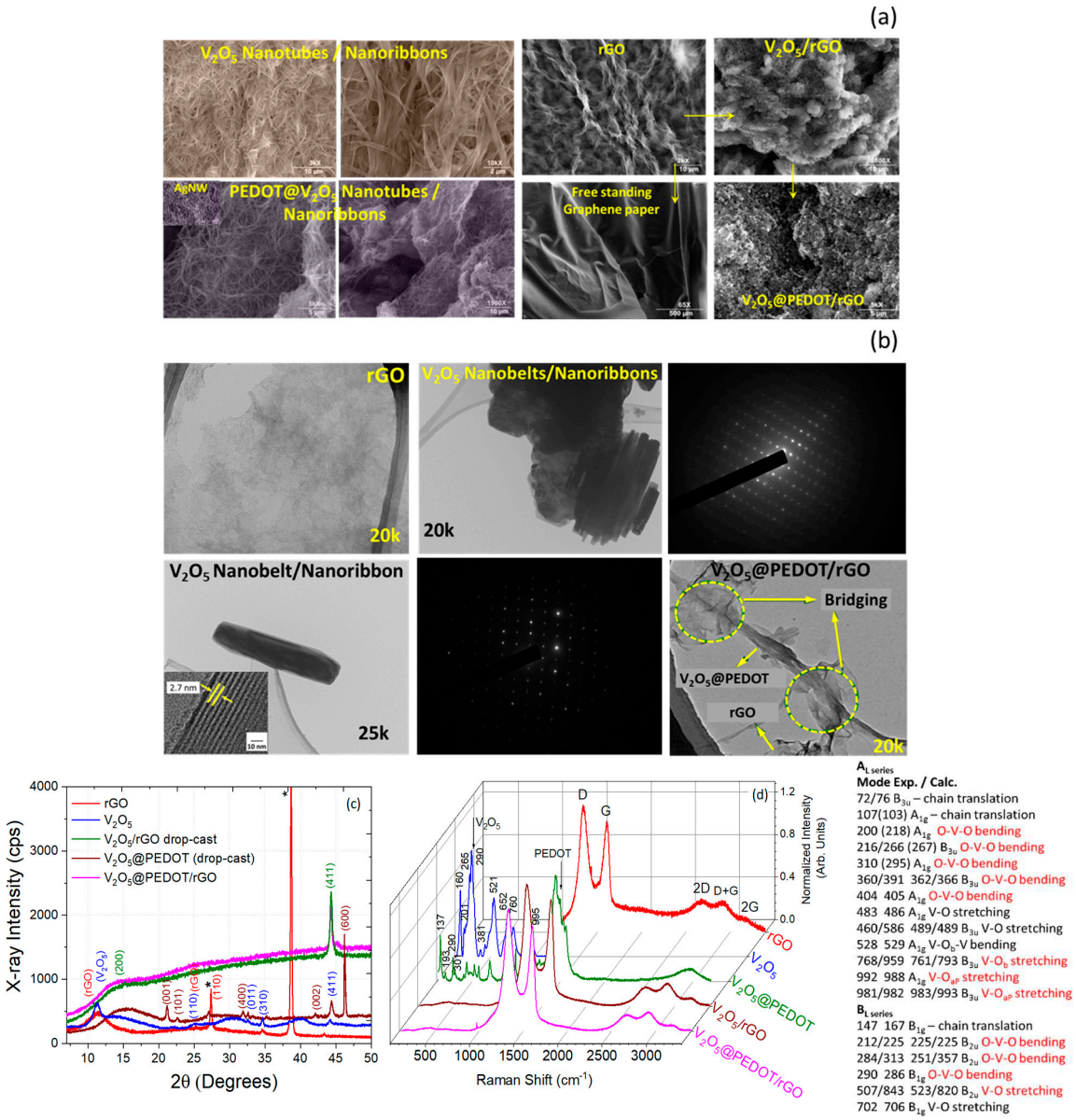

Figure 2. | (a) SEM micrographs for V_2O_5, rGO, V_2O_5@rGO, PEDOT@V_2O_5, free-standing graphene, and V_2O_5@PEDOT/rGO revealing surface morphology. (Scale bars shown at the bottom of the images in μm). (b) TEM images revealing morphology at nanoscale along with SAED pattern of rGO, V_2O_5, and V_2O_5@PEDOT/rGO. (Scale bar: 100 nm and 10 nm). (c) X-ray diffractograms displaying characteristic peaks for graphene (002) and V_2O_5 along with substrate (marked*). (d) Micro-Raman spectra showing characteristic peaks associated with rGO, V_2O_5 nanobelts and PEDOT, for V_2O_5@PEDOT and V_2O_5@PEDOT/rGO. The lattice vibration Raman spectral bands assignment is provided. (Gupta et al.).

The microstructure and distribution of V_2O_5@PEDOT/rGO are studied by scanning electron microscopy (SEM) and transmission electron microscopy (TEM) along with selected area electron diffraction (SAED) showing crystallinity. The strong conjugation inside V_2O_5@PEDOT/rGO endows the adhesion of V_2O_5@PEDOT on the reduced graphene oxide nanosheet and the formation of chemical bridging depicted in Figure 2a,b, which is believed to be important for transferability of hybrid films. SEM showing V_2O_5 nanoribbons, multiplexed with PEDOT and crinkled nanosheets of graphene paper is apparent. The TEM images (Figure 2b) indicate that the width of the as-synthesized V_2O_5@PEDOT nanobelts is around 60 nm. The thickness is about 8.4 nm based on the observation by AFM (not shown). After chemical hybridizing with rGO, the distance between V_2O_5@PEDOT and rGO is estimated to be 0.5 nm, showing a close stacking. The imaging results also demonstrate the

 doi:10.20944/preprints202301.0172.v1

conformal distribution of V_2O_5 and PEDOT, and the coexistence of rGO and V_2O_5@PEDOT in the resulting products. In this work, the maximum d-spacing of 3.96 Å of V_2O_5 [peak (101)] in the XRD pattern (Figure 2c) indicates the absence of intercalated EDOT monomer into V_2O_5 layers [47]. V_2O_5 is a layered compound in which V_2O_5 monolayers are held together by van der Waals forces. Thus, EDOT monomers were polymerized into PEDOT coated on the surface of V_2O_5 nanobelts, instead of intercalating into the interlayer of V_2O_5 leading to formation of core-shell like V_2O_5@PEDOT nanobelts. Evidence of conjugation interaction between V_2O_5@PEDOT and rGO come from Raman spectroscopy. The XRD peak of pristine rGO is somewhere in-between GO precursor and of graphene. The XRD peaks of V_2O_5 are quite narrow exhibiting higher crystallinity, and their position is indicative of primarily α-V_2O_5 phase matched the corresponding pattern (JCPDS Card No. 89-0612). The XRD patterns of hybrids contain peaks related to both rGO and V_2O_5 nanobelts. The peaks at 11.2°, 15.1°, 22.2°, 25.9°, 28.5°, 32.0°, and 41.7°, 44.1° and 46.5° correspond to the (200), (101), (110), (111), (002), (411), and 600) crystal planes of V_2O_5, respectively [48]. The interlayer distance of graphene-conjugated V_2O_5 nanobelts at the (200) reflection (d_{101}) calculated to be 0.405 nm [49,50]. The peak at 12.2° is assigned to partially reduced rGO [51–53]. Interestingly, the peaks related to V_2O_5 show sharp characteristic peaks in hybrids. In the Raman spectra of both V_2O_5@PEDOT and V_2O_5@PEDOT/rGO (Figure 2d), typical peaks at 137, 193, 290, 381, 652 and 995 cm^{-1} confirm the presence of V_2O_5 [54]. The bands at 432, 1371, 1433, and 1564 cm^{-1} can be assigned to the SO_2 bending, C_β–C_β stretching, symmetric C_α=C_β(– O) stretching, and asymmetric C_α=C_β stretching of PEDOT, respectively [55]. Notably, the characteristic peak for graphene nanosheets (G-band associated with sp^2 C) after coupling with V_2O_5@PEDOT (Figure 2d) shifts from 1596 cm^{-1} to a higher frequency of 1610 cm^{-1}, indicating the *p*-type doping of rGO and conjugation between PEDOT and rGO sheet surface [56]. Various other modes belonging to V_2O_5 related to A_L and B_L series are also listed as a side table and for rGO include D (disorder-activated), 2D (intrinsic to sp^2 C systems) and D+G combination bands are also apparent. Moreover, both the samples before (V_2O_5@PEDOT) and after (V_2O_5@PEDOT/rGO) assembling with rGO contain the mixed valences of vanadium (V^{4+} ←→ V^{5+}) manifesting that V_2O_5 is reduced during polymerization process of PEDOT layer.

Transparency and Transferability of V_2O_5@PEDOT/rGO

To obtain high-quality V_2O_5@PEDOT/rGO with both high optical transparency and electrochemical performance, the mass ratio of V_2O_5@PEDOT and rGO has been tuned and optimized. By increasing the V_2O_5@PEDOT content, the optical transparency decreased gradually observed. Even then, all the hybrid films exhibit a high transparency of more than 60% approximately. It is worth noting that the as-formed V_2O_5@PEDOT/rGO hybrid film can be easily transferred onto PET film (see Figure 1), also promising for scalability. The excellent transferability of the V_2O_5@PEDOT/rGO films is attributed to strong affinity between V_2O_5@PEDOT and rGO. Importantly, the hybrid films could be transferred without modifying their shapes. More attractively, the V_2O_5@PEDOT/rGO film is transferable to any different transparent flat and even curved substrates, including PET, ITO, plastic, and glass. Such a substrate-versatile transferable feature of the V_2O_5@PEDOT/rGO is appealing for efficient electronics manufacturing and device integration. Besides, after bending, no visible morphological change was observed by naked eyes suggesting the outstanding flexibility of the V_2O_5@PEDOT/rGO hybrid film. The thickness of the V_2O_5@PEDOT/rGO film was estimated by AFM to be around 33 nm. The linear dependence of transparency on the thickness verified that the tunable transparency of hybrid films ranging from above 60% to 42%.

Electrochemical Properties

To evaluate the electrochemical performance of electrodes, Ag nanowires conductive networks on PET with a high transparency and low sheet resistance of 10 Ω sq^{-1} were prepared via spin coating and used as the transparent conductive substrates. Figure 3 shows representative electrochemical properties of rGO, V_2O_5 nanoribbons, and V_2O_5@PEDOT/rGO in terms of cyclic voltammetry (CV) [(Figure 3a–c)] and galvanostatic charge−discharge (GCD) [(Figure 3i–k)] curves with varying scan rate and current density in aqueous and organic (Figure electrolytes containing Li ions. The as-

Preprints (www.preprints.org) | NOT PEER-REVIEWED | Posted: 10 January 2023 doi:10.20944/preprints202301.0172.v1

prepared transparent electrodes show quasi-rectangular shapes superposed with broad redox peaks related to V_2O_5@PEDOT confirming the double-layer electrochemical capacitance and quasi-triangle shapes (Figure 3i–k), indicating an ideal capacitive and pseudocapacitive behaviors with resistive behavior at the end of the potential window arising from the current carrying substrates as well as solution resistance. While it is observed that for thicker electrodes the areal capacitance tends to be higher, but it declines transparency. Therefore, in this work, the results are reported for around 60% transparent electrodes which are much thinner. At low scan rate of 5-10 mV. s^{-1}, a pair of redox peaks at –0.38 and +0.50 V are assigned to the redox reaction of V_2O_5 [28], suggesting majority of capacity is originated from the V_2O_5@PEDOT composite. At the scan rates of 5, 10, 20, 50, 100, 200, and 500 mV s^{-1}, good capacitive properties are realized, which are consistent with the GCD results GCD curves at current density 5.3 $A.m^{-2}$ (Figure 4e,h). Owing to the presence of high-capacitance V_2O_5@PEDOT without sacrificing its transparency, the transparent electrodes based on V_2O_5@PEDOT/rGO and AgNW networks exhibit superior electrochemical performance compared to those reported earlier.

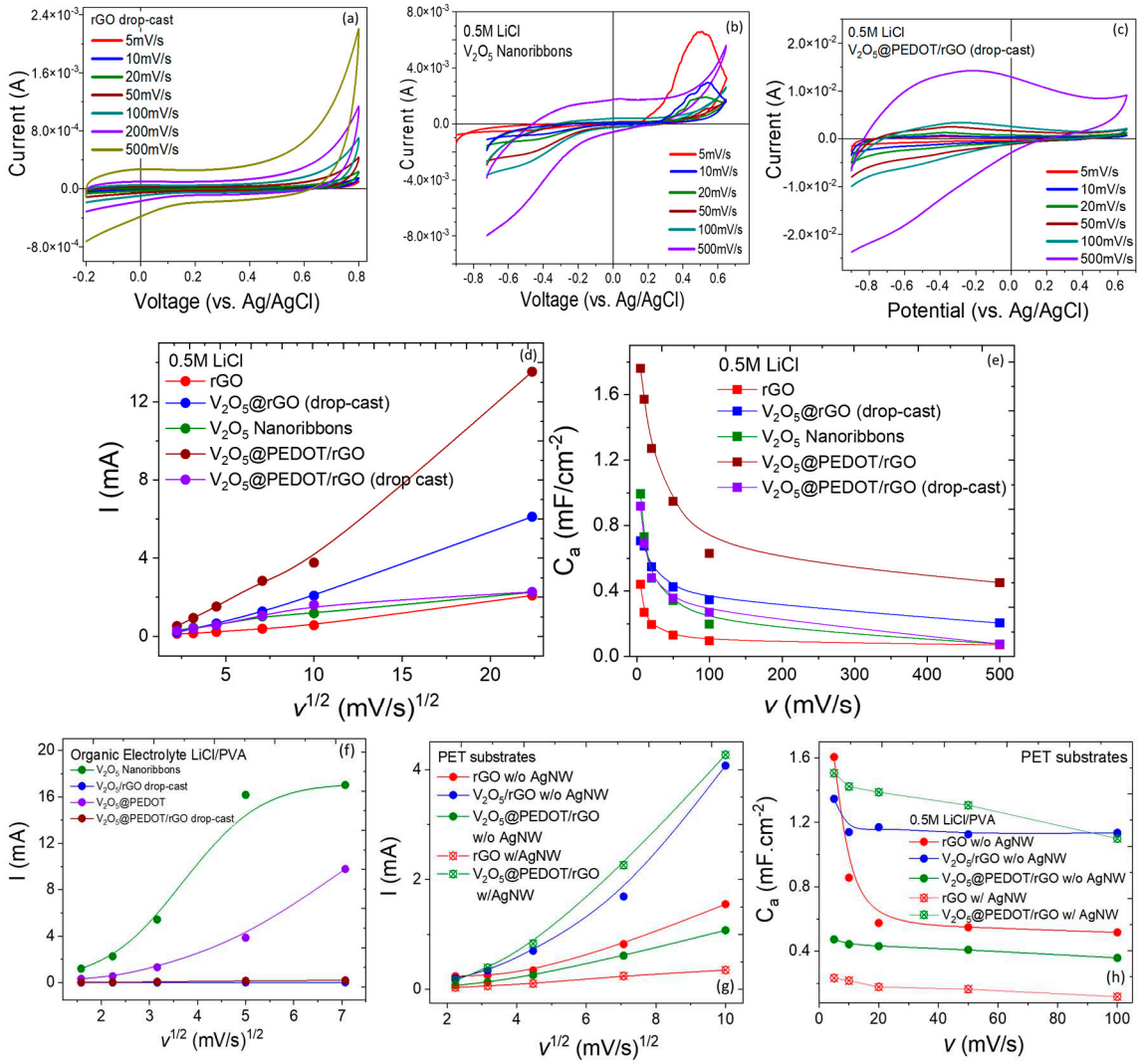

Preprints (www.preprints.org) | NOT PEER-REVIEWED | Posted: 10 January 2023 doi:10.20944/preprints202301.0172.v1

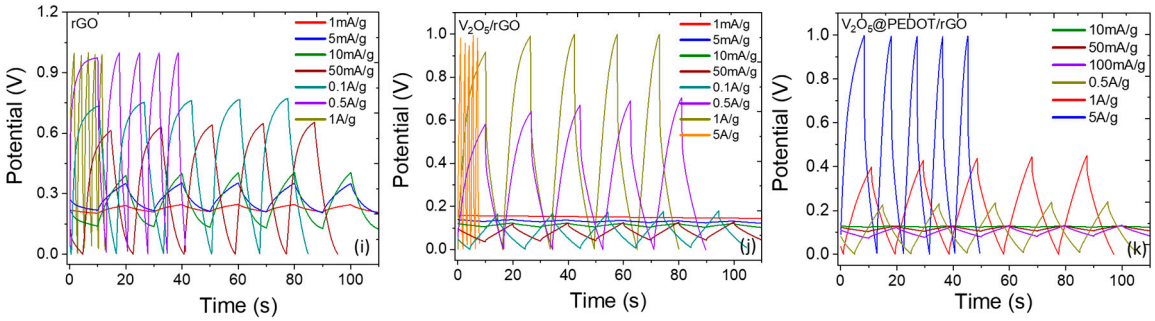

Figure 3. | Electrochemical performance. (a-c) Potentiodynamic cyclic voltammetry (CV) in aqueous electrolyte showing quasi-rectangle behavior with redox peaks. (d, e) Current versus *sqrt* scan rate showing quasi-linear behavior and specific areal capacitance (C_a; mF.cm^{-2}) with scan rate in aqueous electrolyte. (f-h) Current versus *sqrt* scan rate for electrodes without and with AgNW and specific areal capacitance (C_a; mF.cm^{-2}) with scan rate in organic electrolyte. (i-k) Representative galvanostatic charging-discharging (GCD) V-t profiles with varying current density for rGO, V_2O_5@rGO and V_2O_5@PEDOT/rGO. (Gupta et al.).

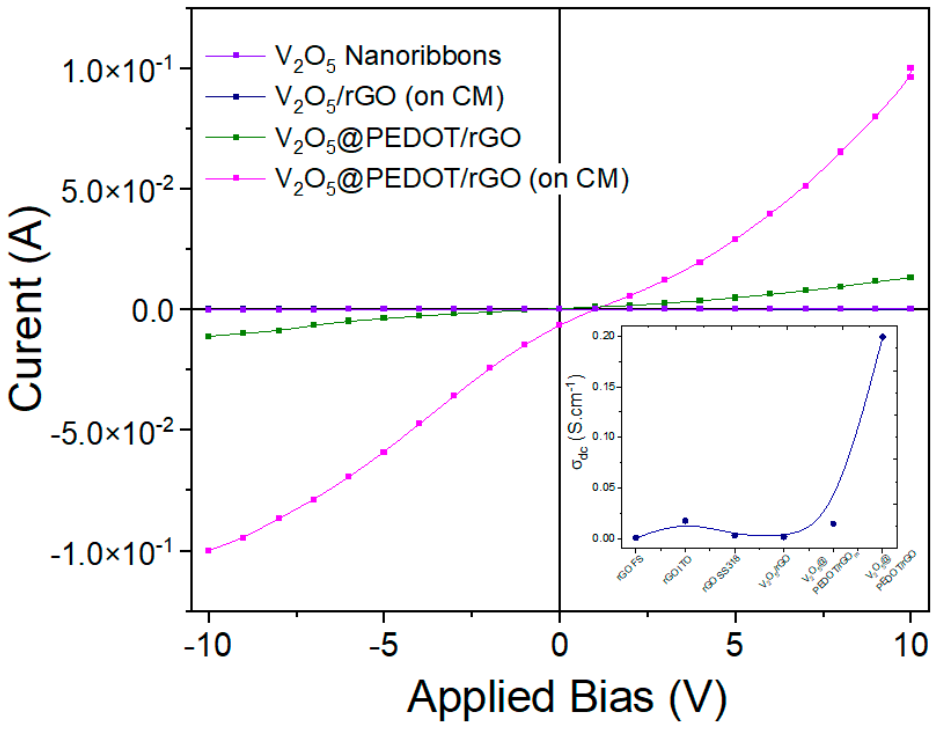

Figure 4. | Room temperature electrical (I-V) properties and dc conductivity for all electrodes. (Gupta et al.).

Qualitatively, CV curves for hybrids indicate they have higher specific areal capacitance (C_a). According to CV (and GCD) results, the calculated areal capacitance C_a is as high as 1.6 mF.cm^{-2} at 5 mV/s (and 0.5A/g or 0.1 A.m^{-2}) in 0.5M electrolyte concentration, which is higher than that of Au/MnO_2 [57], graphene [58], ITO/PDDA/MoS_2 [59,60], ITO/MnO_2 [61,62], and other transparent electrodes, demonstrating the superiority of the present V_2O_5@PEDOT/rGO ternary hybrid electrodes. Important to note that these electrodes possess higher C_a values than those of constituents. Electrochemical properties also showed that C_a decreased with scan rate for both the electrolytes as anticipated (Figures 3e,h). The rGO nanosheets provide high electrical conductivity of 0.2 S/cm (see Figure 4) and mechanical robustness and the addition of rGO with V_2O_5 nanobelts provides larger surface area, which further enhances the double-layer non-faradaic process of the hybrids. The *V-t*

Preprints (www.preprints.org) | NOT PEER-REVIEWED | Posted: 10 January 2023 doi:10.20944/preprints202301.0172.v1

profiles between 0 and 1.0 V at different current densities and cyclability of electrodes exhibit stable performance for more than 1000 cycles. The fading in C_a is due to internal resistance and polarization of the electrodes. The rate capability is strongly influenced by ion diffusion in the electrolyte, the surface adsorption of ions on the electrode materials (electrode/electrolyte accessibility) and the charge transfer on the electrode. At higher scan rates, any of these three processes are rate-limiting, lowering the C_a. Figure 3d,f,g show variation of maximum current with square root of scan rate ($v^{1/2}$), depicting quasi-linear behavior, especially at higher scan rates, which is reminiscence of diffusion-limited (mass transport) phenomena and reflective of heterogeneous electron transfer ascribed to the composite nature of hybrid electrodes. Quantitatively, the magnitude of the current is governed by the Randles–Ševćik equation [4,63]: $I_{rev} = (2.69 * 10^5) n^{3/2} AC\, D^{1/2}\, v^{1/2}$ - (1), where A is geometric area of electrode (cm^2), F the Faraday constant ($C \cdot mol^{-1}$), D the diffusion coefficient (cm^2/s), C the concentration (mol/cm^3), v the scan rate (V/s), R and T are the usual physical constants, and n (=1) is the number of electrons transferred in the electrochemical process ($V^{5+} + e^- \leftrightarrow V^{4+}$). Through the analysis of current we determined D that ranged between $0.1 \times 10^{-6} – 1 \times 10^{-6}$ $cm^2 \cdot s^{-1}$ for all the samples studied. There is an obvious increase in D values for V_2O_5@PEDOT/rGO as opposed to rGO nanosheets, V_2O_5 and V_2O_5@PEDOT which is attributed to tunable surface morphology at nanoscale, permitting access to numerous hydrophilic edges, basal plane defects and surface functional groups.

Nevertheless, the higher specific capacitance is attributed to smaller size vanadium pentoxides nanobelts, resulting in high specific capacitance. Although rGO nanosheets have a supplementary (supercapacitive) contribution to the hybrids, they have excellent electronic conductivity and, thus, shuttle the electrons between vanadium-oxide nanostructures and the current collector. Therefore, the chemical integration between rGO-V_2O_5 nanobelts into a single system enhanced the electrochemical behavior of pseudocapacitive electrodes. The synergistic effects of chemical bridging (utilizing electrostatic and coordination interactions between negatively charged surface functional groups of rGO and V^{4+}/V^{5+} ions), the crumpled and flower-like surface morphology promoted tailored properties and interfaces and topologically interconnected network architectures. We attribute this enhancement to the concomitant double-layer or non-Faradaic capacitance and pseudocapacitive (redox) electrochemical processes on the addition of rGO with V_2O_5@PEDOT (V_mG_n) composite materials. Moreover, V_2O_5 has layered crystal structure from XRD and multivalent vanadium oxidation states. These properties facilitate the insertion and extraction of alkali-metal electrolyte ion (Li^+) in the vicinity of the electroactive material. The ion insertion process can be expressed as follows [29]: $V_2O_5 + xLi^+ + xe^- \leftrightarrow V^{5+}_{2-x} Li^+_x V^{4+}_x O^{2-}_5 + xLi^+$ (see Figure 1). From Equation, the charging-discharging processes involve reversible intercalation of Li^+ into layered V_2O_5 with simultaneous electron transfer *i.e.,* the partial reduction of V^{5+} to V^{4+} (or vice versa) during redox reaction and thus provides pseudocapacitance to V_xG_y hybrids. It is known that the electrodes based on V_2O_5 suffer from the capacity decay in neutral aqueous electrolytes due to the formation of soluble vanadium species, including $V^{3+}, VO^+, VO^{2+}, H_2VO_4^-, and\ HV_2O_5^-$ [33]. Surprisingly, the as-prepared transparent electrodes exhibited an outstanding durability over 1000 cycles with a slight increase in capacitance during the long-term cycling.

Electrochemical Imaging and Determination of Heterogeneous Electron Transfer Rate

To further confirm the synergistic effects between the coating layer of PEDOT and rGO, scanning electrochemical microscopy (SECM) is used that allows to monitor physicochemical properties (diffusion kinetics), to probe charge transfer and ion transport dynamics and to obtain quantitative information of heterogeneous electron transfer (k_{HET}), as well as determine electroactive adsorption sites density at nanoscale using microelectrode. By detecting redox surface reactions, SECM can map ionic currents and chemical reactivity correlating with surface topography as opposed to other scanning probe microscopy. Figure 5 shows cyclic voltammograms (CV) measured in microelectrode (convergent diffusion) configuration in a single-compartment, three-electrode electrochemical cell with Pt tip in 0.5M LiCl (aqueous; Figure 5a and organic; Figure 5b) electrolytes and 5mM $K_3Fe(CN)_6$ (potassium ferricyanide) redox probe between −0.9V and +0.6V at scan rate 20 mV/s. In traditional macroelectrode, the redox reactions occur across the entire electrode surface so that ion diffusion

Preprints (www.preprints.org) | NOT PEER-REVIEWED | Posted: 10 January 2023 doi:10.20944/preprints202301.0172.v1

appears planar and the CV response current show 'diffusion-limited' behavior (see Figure 3). However, diffusion to or from the edge of macroelectrode is effective only to a point and therefore current density and mass transport rate are larger at the edge and diffusion becomes convergent (equivalent of microelectrode), which is the case in SECM. Qualitatively, the CV loop was sufficiently rectangular, reminiscent of a supercapacitor, and the traditional electrode cyclic voltammograms highlight unique difference in signal features (Figure 5b, inset) and current magnitude.

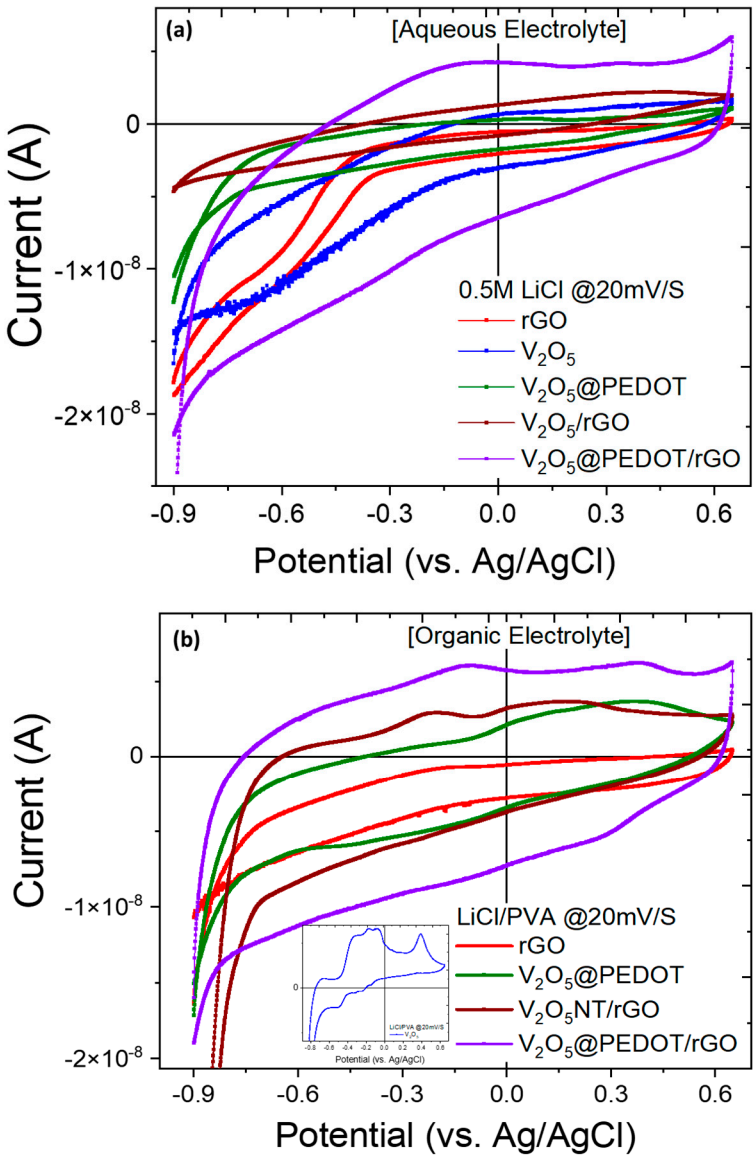

Figure 5. | Cyclic voltammetry (CV) curves measured using SECM micro-electrodes of as-prepared samples in (a) aqueous and (b) organic electrolytes showing characteristic redox peaks. (Gupta et al.).

Since the redox probed used in this study is surface-sensitive, it enables to distinguish different surface functionality at nanoscale, which is usually not possible with outer-sphere ruthenium hexamine (Ru $(NH_3)_6$ redox probe [64–66]. We determined first-order heterogeneous electron transfer rate (k_{HET}) following probe approach technique in feedback mode for all the electrodes. The tip was polarized at +0.4V potential to ensure electrochemical redox reaction (tip generation) and the current was recorded (substrate collection) over the polarized electrode surfaces (±0.5V), naming Pol1 and Pol2, to determine k_{HET} and visualize electroactivity in feedback mode. Figure 6 shows probe approach curves with normalized tip current and substrate (WE)–probe tip distance ($L=d/a$). A Pt

Preprints (www.preprints.org) | NOT PEER-REVIEWED | Posted: 10 January 2023 doi:10.20944/preprints202301.0172.v1

ultramicroelectrode (radius, a=10.0 μm) with RG=2 was adopted as the SECM tip. The tip current (i_T) reaches asymptotic behavior with steady-state current following: $i_{T,\infty=4nFCDa,}$ where n is the number of electrons transferred, C the concentration or flux of oxidized species and D the diffusion coefficient limited by hemispherical region. The feedback current of the tip is dependent upon HET capability of the local electrode area. When L=d/a ≤ 1, the normalized feedback current increases gradually. With the tip approaching the conductive surface, the reduced species formed at the tip is oxidized, resulting in increased tip current: $i_T > i_T^{cond} = \frac{i_T}{i_{T,\infty}} = \left[k_1 + \frac{k_2}{L} + k_3 \exp(\frac{k_4}{L})\right] - (2)$ and creates a regenerative "positive" feedback loop. The opposite effect is observed when approaching an insulating (or semiconducting) region and diffusion is inhibited due to physical obstruction creating "negative" feedback loop and decreasing the tip current i.e. $i_T < i_{T,\infty}$, $i_T^{ins} = \frac{i_T}{i_{T,\infty}} = \frac{1}{\left[k_1 + \frac{k_2}{L} + k_3 \exp(\frac{k_4}{L})\right]} -$ (3) [20,58]. The probe approach curves were fitted as dashed curved in Figure 6 for both aqueous (Figure 6a) and organic electrolytes (Figure 6b). The data points in solid and hatched symbols are from the measurements with two polarities with vertical error bars. The k_{HET} (or k_1 in equations above) values ranged 0.08–4.0 cm. s^{-1} for rGO to V_2O_5@PEDOT/rGO electrodes (Figure 6c) and the values are within 0.5% accuracy that is smaller than experimental uncertainty. These values are higher than those of reported values for pristine CVD graphene layer ($2.0 \times 10^{-2} - 4.2 \times 10^{-2}$) in aqueous solution [40]. The difference is due to tunable morphology, defects density, edge sites, and pseudocapacitive elements in hybrids. The Figure 6c displays the correlation between k_{HET} and D for all the electrodes in both the electrochemical environment following V_2O_5@PEDOT/rGO in organic electrolyte the highest and rGO in aqueous electrolyte the lowest. These results are attributed to overall satisfactory performance arising due to the synergistic effects from supercapacitive graphene as elastic and electrically conductive matrix and pseudocapacitive V_2O_5 nanobelts with PEDOT allowing faster ion transport across Li-based electrolytes.

In general, electrolytes determine the stability of the device controlling its potential for supercapacitor operation useful in peak power applications to suppress and compensate transient effects, however, suffer from self-discharge due to the redox reactions process. Liquid organic electrolytes are the basic form of organic electrolytes in which conductive salt (LiCl in this study) is added to the gel solvent (polymeric PVA in this study). In our hybrid composite electrodes, it is believed that PEDOT function as insulating layer (blocking layer) on the supercapacitors' performance. Density functional theory (DFT) calculations also reported that in the presence of PEDOT coating of a few nanometers, the enlarged energy barriers of 19.3 eV, 14.7 eV and 13.6 eV are subsistent for V-containing (V^{3+}, VO^{+}, and VO^{2+}) amphoteric species, respectively, much higher than that of pristine V_2O_5. With such a sizeable energy barrier, the penetration of these ions across the PEDOT layer is unfavorable demonstrating the chemical blocking effect of PEDOT upon them [67]. The conjugated rGO further prevents the V-containing species from dissolving into the electrolytes by trapping the soluble V-based ions, boosting unusual cycling durability of the V_2O_5@PEDOT/rGO. Thus, by balancing electronic conductivity by chemical bridging and effective blocking by thin PEDOT layer, the optimal k_{HET} via SECM is achieved. The SECM images (400 μm × 400 μm) as in Figure 7 displays probe current distribution as two-dimensional contour "heat maps" and three-dimensional images with occasional higher/lower current reflecting "reactive" electroactive site distribution. It is clearly observed that the normalized feedback current is different from each other and to those of reduced graphene oxide promoted by the presence of defects density, and pseudocapacitive metal oxides and conducting polymers as they depended on surface morphology. Conventional wisdom indicates that higher is the feedback current, the faster is the local HET rate. It is apparent that the samples yielded regions of higher electroactive regions with areal site density (~30–50 μm^2). These findings underscore the significance of inherent complex structure.

Preprints (www.preprints.org) | NOT PEER-REVIEWED | Posted: 10 January 2023 doi:10.20944/preprints202301.0172.v1

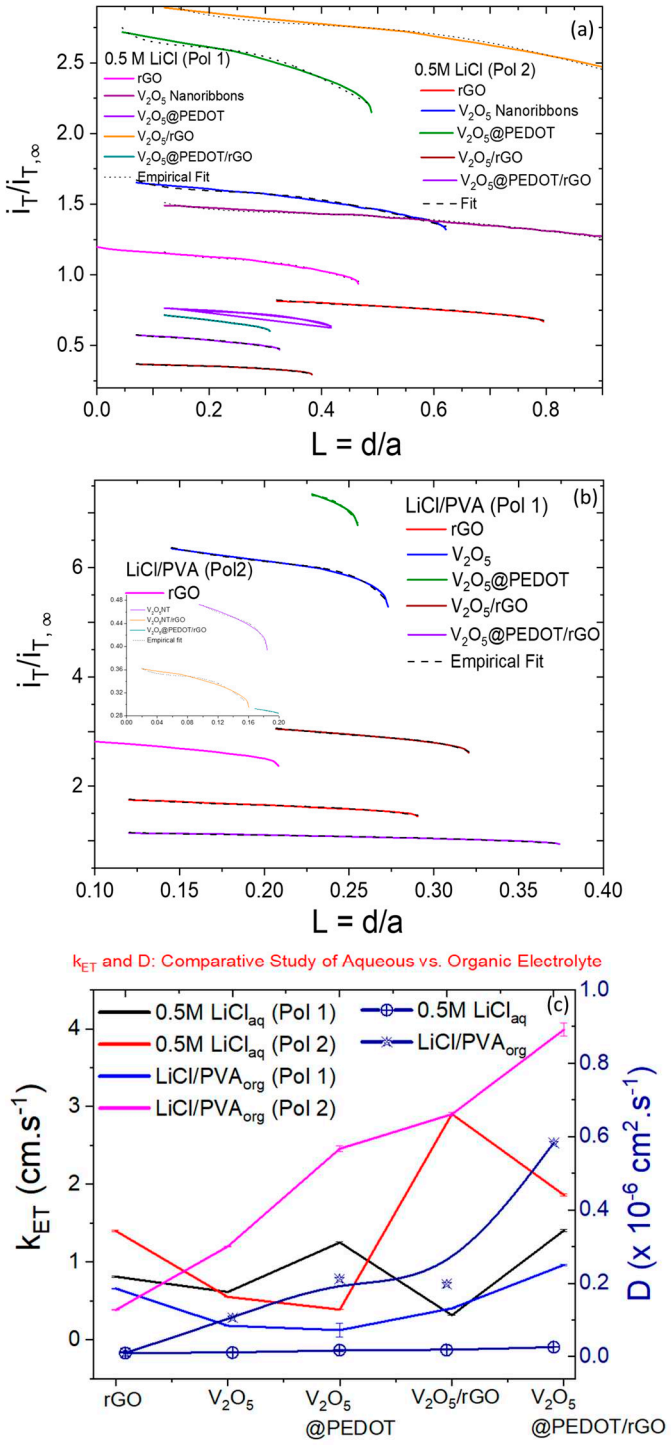

Figure 6. | Probe approach curves showing normalized tip current, and distance measured at polarity 1 (Pol 1: V_t=+0.4V, V_s=-0.5V) and polarity 2 (Pol 2: V_t=+0.4V, V_s=+0.5V) showing semiconducting behavior for all electrodes in (a) aqueous and (b) organic electrolytes and empirical fit. (c) Variation of electron transfer rate k_{HET} and diffusion coefficient (D) for all electrodes in different electrochemical environment. (Gupta et al.).

Preprints (www.preprints.org) | NOT PEER-REVIEWED | Posted: 10 January 2023 doi:10.20944/preprints202301.0172.v1

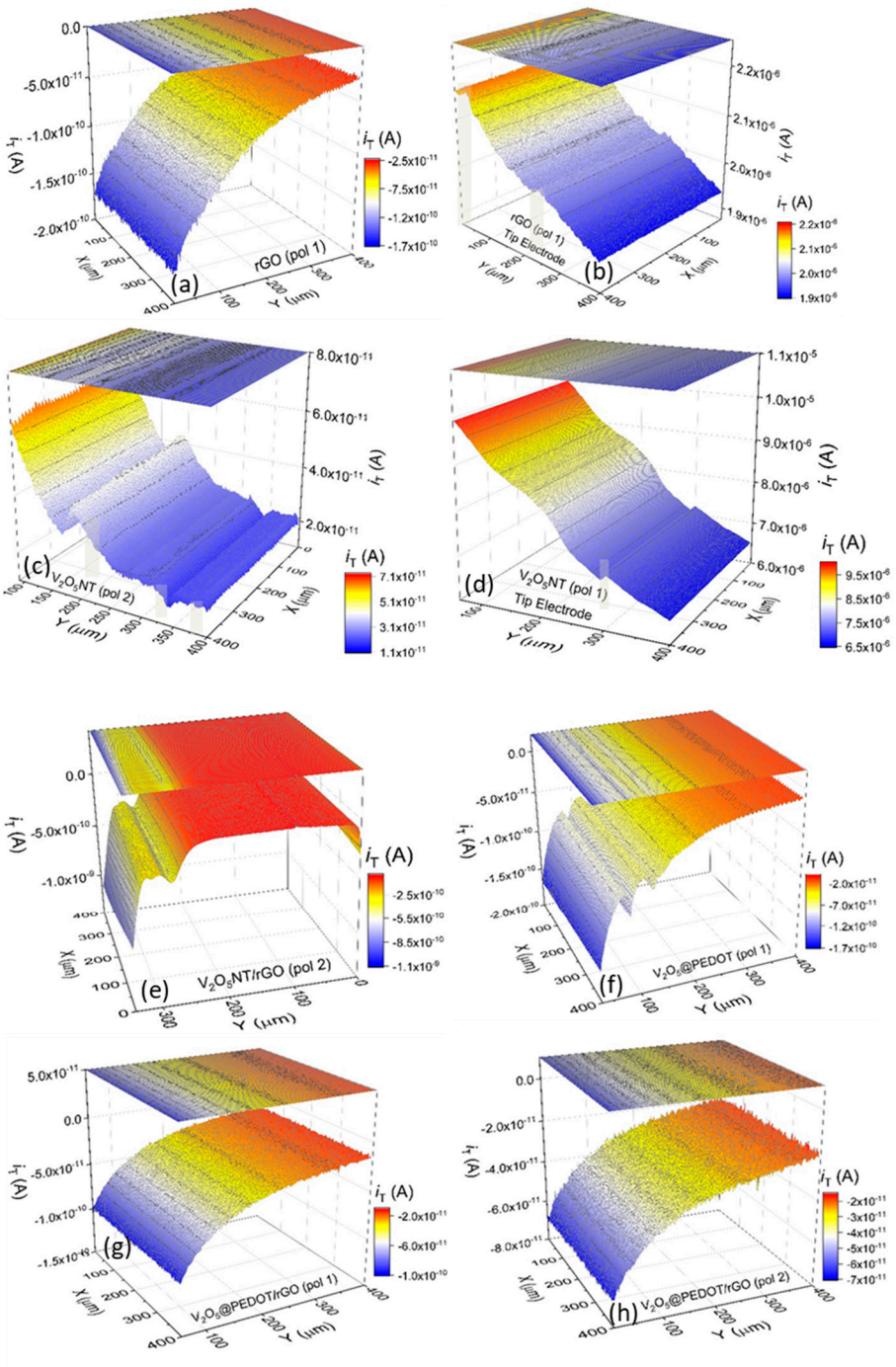

Figure 7. | SECM mapping in two- and three-dimension for (a) rGO (Pol 1), (b) rGO (tip electrode, Pol 1), (c) V_2O_5 (Pol 2), V_2O_5 (tip electrode, Pol 1), (e) V_2O_5/rGO (Pol 2), (f) V_2O_5@PEDOT (Pol1), (g) V_2O_5@PEDOT/rGO (Pol 1), and (h) V_2O_5@PEDOT/rGO (Pol 2), showing regions of high to moderate and low electroactivity. (Gupta et al.).

Theoretical Considerations for Correlated HET Rates

In general, the redox states are electronically coupled to the electrolyte leading to a crossing event of wavefunctions at which tunneling may occur, also based on the microscopic theory of coupled ion-electron transfer facilitating non-adiabatic electron transfer. The concerted ion-electron transfer requires that ions and electrons of the reactant system to be transferred concomitantly to form complex product. The heterogeneous rate, k_{HET} between electrode and redox probe $K_3Fe(CN)_6$ is described by Gerischer-Marcus model [68]: $k_{HET} = v_n \int \varepsilon_{red}(E) f(E) DOS_{el}(E) W_O(\lambda, E) dE - (4)$, where $W_o(\lambda, E) = \frac{1}{\sqrt{4\pi kT}} \exp\left(-\frac{(E-(E^o+\lambda))^2}{4\lambda kT}\right) - (5)$, v_n the nuclear frequency factor, ε_{red} (E) is the

Preprints (www.preprints.org) | NOT PEER-REVIEWED | Posted: 10 January 2023 doi:10.20944/preprints202301.0172.v1

proportionality factor, f(E) the Fermi function, DOS_{el} the density of states of electrode, $W_o(\lambda, E)$ the probability density function of the oxidized (unoccupied) states and λ is the reorganization energy of $K_3Fe(CN)_6$ [reduction] in solution. The electron transfer kinetics is related to the integration of uncoated rGO electronic states and those of hybrids and oxidized states of $K_3Fe(CN)_6$ near the Fermi level. The DOS is insufficient near the Fermi energy (E_F) for pristine graphene unlike rGO. With the induction of partial oxygenated functionalities, defects induced localized mid gap states is observed that enlarge the overlap, which facilitates higher HET from graphene-based hybrids and $K_3Fe(CN)_6$ [69,70]. The rate formula is applicable to Li-based electrolytes, where reduction of the electrode couples with ion insertion. These results pave the way for interfacial engineering to enhance ion intercalation rates, not only for supercap-batteries, but also for ionic separation.

Electrochemical Performance of Transparent Symmetric Devices

Inspired by the encouraging results achieved in transparent electrodes, we assembled symmetric solid-state supercapacitors which are also transparent. The CV curves were similar to each other as well as the GCD curves, showing a good capacitive behavior. Besides, high areal capacitances of 0.4-0.6 $mF.cm^{-2}$ at 20 $mV.\ s^{-1}$ and 1.7 $mF.cm^{-2}$ at a current density of 0.05 $A.m^{-2}$ were achieved.

Conclusions

In summary, we successfully demonstrated the fabrication of rGO conjugated V_2O_5@PEDOT ternary composite films via chemical solution method, which featured several intriguing characteristics including synergistic effects between PEDOT and rGO and V_2O_5@PEDOT/rGO endow with good cycling durability. Furthermore, the versatile and transparent symmetric solid-state supercapacitors based on V_2O_5@PEDOT/rGO delivered the highest energy density of 0.27 $\mu Wh.cm^{-2}$ and good chemical stability, showing their potential for applications in future transparent electronics. As demonstrated by experimental results, both the kinetic blocking of the PEDOT (insulating) layer preventing self-discharge and the anchoring capability of graphene-like nanosheets in LiCl/PVA gel electrolyte prevent amphoteric soluble vanadium ions from V_2O_5 nanoribbons/nanotubes by minimizing water content and providing a neutral pH medium that contribute synergistically to the unusual electrochemical stability and electroactivity shown using scanning electrochemical microscopy; SECM. It also serves as a matrix to maintain the V2O5 nanoribbon network structure. Combination of electrode kinetics using macro-electrochemistry and first-order electron transfer rate (k_{HET}) from SECM helped to establish correlations for a range of nanomaterials following V_2O_5@PEDOT/rGO the highest and rGO the lowest in this study. We attributed the overall superior performance due to synergistic effects from supercapacitive reduced graphene oxide with larger surface area as mechanically robust and electrically conductive platform and pseudocapacitive V_2O_5 nanobelts with PEDOT allowing faster ion transport across Li-based polymer gel electrolyte.

Author Contributions: Sanju Gupta: Samples synthesis, characterization, investigation (lead); Conceptualization & methodology (lead); data interpretation, resources (lead); writing-original draft, review, and editing (lead). **Brendan Evans:** Samples synthesis, characterization, Analysis, writing. All authors have read and agreed to the published version of the manuscript.

Data Availability Statement: The data that support the findings of this study are available within the article.

Acknowledgments: The authors gratefully acknowledge support in parts from KY NSF EPSCoR, KY NASA EPSCoR, and internal RCAP-I Award from WKU Research Foundation when both were at WKU. The author (B.E.) also thankful to J. Andersland (Biology, WKU) for electron microscopy training.

Conflicts of Interest: The authors declare that they have no conflict of interest.

 doi:10.20944/preprints202301.0172.v1

References

1. S. Chu, Y. Cui, N. Liu, The path towards sustainable energy. Nat. Mater. 16, 16-22 (2016);
2. M. Armand, Polymer solid electrolytes - an overview. Solid State Ionics 9(10), 745-754 (1983);
3. Y. Shim, H. J. Kim, Y. J. Jung, Graphene-based supercapacitors in the parallel-plate electrode configuration: Ionic liquids versus organic electrolytes. Faraday Discuss. 154, 249-263 (2012).
4. K. Ellmer, Past achievements and future challenges in the development of optically transparent electrodes. Nat. Photon. 6, 809-817 (2012).
5. R. G. Gordon, Criteria for choosing transparent conductors. MRS Bull. 25, 52-57 (2011).
6. C.-C. Kim, H.-H. Lee, K.H. Oh, J.-Y. Sun, Highly stretchable, transparent ionic touch panel. Science 353, 682-687 (2016).
7. T. M. Higgins, J.N. Coleman, Avoiding resistance limitations in high-performance transparent supercapacitor electrodes based on large-area, high-conductivity PEDOT: PSS films. ACS Appl. Mater. Interfaces 7, 16495-16506 (2015).
8. C. F. Zhang, T. M. Higgins, S.-H. Park, S. E. O'Brien, D. Long, J. N. Coleman, V. Nicolosi, Highly flexible and transparent solid-state supercapacitors based on RuO2/PEDOT: PSS conductive ultrathin films. Nano Energy 28, 495-505 (2016).
9. S. De, T. M. Higgins, P. E. Lyons, E. M. Doherty, P. N. Nirmalraj, W. J. Blau, J.J. Boland, J. N. Coleman, Silver nanowire networks as flexible, transparent, conducting films: extremely high DC to optical conductivity ratios. ACS Nano 3, 1767-1774 (2009).
10. Y.-H. Liu, J.-L. Xu, X. Gao, Y.-L. Sun, J.-J. Lv, S. Shen, L.-S. Chen, S.-D. Wang, Freestanding transparent metallic network based ultrathin, foldable, and designable supercapacitors. Energy Environ. Sci. 10, 2534-2543 (2017).
11. G. Li, Y. Liu, H. Zhou, Layered graphite foil/poly(3,4-ethylenedioxythiophene) electrode-enabled flexible electrochemical capacitors with observably boosted performances. J. Electroanal. Chem. 920, 116568-116574 (2022).
12. L. Hu, H.S. Kim, J.-Y. Lee, P. Peumans, Y. Cui, Scalable coating and properties of transparent, flexible, silver nanowire electrodes. ACS Nano 4, 2955-2963 (2010).
13. B. W. Wang, S. Jiang, Q.-B. Zhu, Y. Sun, J. Luan, P.-X. Hou, S. Qiu, Q.-W. Li, C. Liu, D.-M. Sun, H.-M. Cheng, Continuous fabrication of meter-scale single-wall carbon nanotube films and their use in flexible and transparent integrated circuits. Adv. Mater. 30, e1802057 (2018).
14. S. Pang, Y. Hernandez, X. Feng, K. Müllen, Graphene as transparent electrode material for organic electronics. Adv. Mater. 23, 2779-2795 (2011).
15. S. Bae, H. Kim, Y. Lee, X. Xu, J.-S. Park, Y. Zheng, et. al., Roll-to-roll production of 30-inch graphene films for transparent electrodes. Nat. Nanotechnol. 5, 574-578 (2010).
16. K. S. Kim, Y. Zhao, H. Jang, S. Y. Lee, J. M. Kim, K. S. Kim, et. al., Large-scale pattern growth of graphene films for stretchable transparent electrodes. Nature 457, 706-710 (2009).
17. F. Chen, P. Wan, H. Xu, X. Sun, Flexible transparent supercapacitors based on hierarchical nanocomposite films. ACS Appl. Mater. Interfaces 9, 17865-17871 (2017).
18. S. Gupta, C. Price, Investigating graphene/conducting polymer hybrid layered composites as pseudocapacitors: Interplay of heterogeneous electron transfer, electric double layers and mechanical stability. Composites Part B 105, 46-59 (2016).
19. C. F. Zhang, V. Nicolosi, Graphene and MXene-based transparent conductive electrodes and supercapacitors. Energy Storage Mater. 16, 102-125 (2019).
20. S. A. Hasan, J. L. Rigueur, R. R. Harl, A. J. Krejci, I. G.-Juan, B. R. Rogers, J. H. Dickerson, Transferable graphene oxide films with tunable microstructures. ACS Nano 4, 7367-7372 (2010).
21. Y. Jiang, J. Liu, Definitions of pseudocapacitive materials: a brief review. Energy Environ. Mater. 2, 30-37 (2019).
22. B. Saravanakumar, K. K. Purushothaman, G. Muralidharan, High performance supercapacitor based on carbon coated V2O5 nanorods. J. Electroanal. Chem. 758, 111-116 (2015).
23. S. Gupta. S. B. Carrizosa, B. McDonald, J. Jasinski, N. Dimakis, Graphene-family nanomaterials assembled with cobalt oxides and cobalt nanoparticles as hybrid supercapacitive electrodes and enzymeless glucose detection platforms. J. Mater. Res. 32, 301-322 (2017).
24. S. Gupta, M. vanMeveren and J. Jasinski, Investigating Electrochemical Properties and Interfacial of Manganese Oxides/Graphene Hybrids as High-Performance Supercapacitor Electrode Electrochem. Sci. 10, 10272-10291 (2015).
25. S. Bai, K. Zhang, L. Wang, J. Sun, R. Luo, D. Li and A. Chen, Synthesis mechanism and gas-sensing application of nanosheet-assembled tungsten oxide microspheres. J. Mater. Chem. A 2, 7927-7934 (2014).
26. G. Wang L. Zhang, J. Zhang, A review of electrode materials for electrochemical supercapacitors. Chem. Soc. Rev. 41, 797-828 (2012).
27. R. Raccichini, A. Varzi, S. Passerini and B. Scrosati, A. Varzi, S. Passerini, B. Scrosati, The role of graphene for electrochemical energy storage. Nat. Mater. 14, 271 (2015).

Gupta *et al.*
Figure 6.

28. T. O. Wehling, K. S. Novoselov, S. V. Morozov, E. E. Vdovin, M. I. Katsnelson, A. K. Geim, A. I. Lichtenstein, Molecular doping in graphene. Nano Lett. 8, 173–177 (2008).
29. M. Lee, S. K. Balasingham, H.Y. Jeong, W. G. Hong, H.B.-R. Lee, B. H. Kim, Y. Jun, One-step hydrothermal synthesis of graphene decorated V2O5 nanobelts for enhanced electrochemical energy storage. Sci. Rep. 5, 8151:1-8151:8 (2015).
30. J. Wu, X. Gao, H. Yu, T. Ding, Y. Yan, B. Yao, X. Yao, D. Chen, M. Liu, L. Huang, A scalable free-standing V2O5/CNT film electrode for supercapacitors with a wide operation voltage (1.6 V) in an aqueous electrolyte. Adv. Funct. Mater. 26, 6114-6120 (2016).
31. S. Gupta, B. Aberg, S. B. Carrizosa, N. Dimakis, Vanadium Pentoxide Nanobelt-Reduced Graphene Oxide Nanosheet Composites as High-Performance Pseudocapacitive Electrodes: ac Impedance Spectroscopy Data Modeling and Theoretical Calculations. Materials 9, 615:1-615:20 (2016).
32. S. D. Perera, A. D. Liyanage, N. Nijem, J. P. Ferraris, Y. J. Chabal, K. J. Balkus Jr. Vanadium oxide nanowire–Graphene binder free nanocomposite paper electrodes for supercapacitors: A facile green approach. J. Power Sources 230, 130-137 (2013).
33. H.H. Kristoffersen, H. Meitu, Structure and oxidizing power of single layer ◉-V2O5. Topics in Catalysis, 59, 809-816 (2016).
34. A.M. Engstrom, F.M. Doyle, Exploring the cycle behavior of electrodeposited vanadium oxide electrochemical capacitor electrodes in various aqueous environments. J. Power Sources 228, 120-131 (2013).
35. J. W. Lee, S.Y. Lim, H.M. Jeong, T.H. Hwang, J.K. Kang, J.W. Choi, Extremely stable cycling of ultra-thin V2O5 nanowire–graphene electrodes for lithium rechargeable battery cathodes. Energy Environ. Sci. 5, 9889-9894 (2012).
36. Q. T. Qu, Y.S. Zhu, X.W. Gao, Y.P. Wu, Core-shell structure of polypyrrole grown on V2O5 nanoribbon as high-performance anode material for supercapacitors. Adv. Energy Mater. 2, 950-955 (2012).
37. M. Yu, Y. Zeng, Y. Han, X. Cheng, W. Zhao, C. Liang, Y. Tong, H. Tang, X. Lu, Valence-optimized vanadium oxide supercapacitor electrodes exhibit ultrahigh capacitance and super-long cyclic durability of 100 000 cycles. Adv. Funct. Mater. 25, 3534-3540 (2015).
38. S. Gupta, N. Dimakis, Computational predictions Computational predictions of electronic properties of graphene with defects, adsorbed transition metal-oxides and water using density functional theory. Appl. Surf. Sci. 467-468, 760-772 (2017) and references therein.
39. P. Simon, Y. Gogotsi, Materials for electrochemical capacitors. Nat. Mater. 7 (2008) 845–854 (2008) and references therein.
40. J. Han, S. Yuan, L. Liu, X. Qiu, H. Gong, X. Yang, C. Li, Y. Hao, B. Cao, Fully indium-free flexible Ag nanowires/ZnO: F composite transparent conductive electrodes with high haze. J. Mater. Chem. A3, 5375-5384 (2015).
41. L. Wang, H. Yang, X. Liu, R. Zeng, M. Li, Y. Huang, X. Hu, Constructing hierarchical tectorum-like α-Fe2O3/PPy nanoarrays on carbon cloth for solid-state asymmetric supercapacitors. Angew. Chem. Int. Ed. 56, 1105-1110 (2017).
42. Y. Zhong, X. Zhang, Y. He, H. Peng, G. Wang, G. Xin, Simultaneously armored and active graphene for transparent and flexible supercapacitors. Adv. Funct. Mater. 28, 1801998- (2018).
43. W. Li, C. Tan, M. A. Lowe, H. D. Abruňa, D. C. Ralph, Electrochemistry of Individual Monolayer Graphene Sheets. ACS Nano 5, 2264-2270 (2011).
44. S. Gupta, S. B. Carrizosa, Insights into electrode/electrolyte interfacial processes and the effect of nanostructured cobalt oxides loading on graphene-based hybrids by scanning electrochemical microscopy. Appl. Phys. Lett. 109, 243903-243905 (2016) and references therein.
45. J. -L. Xu, Y.-H. Liu, X. Gao, Y. Sun, S. Shen, X. Cai, L. Chen, S.-D. Wang, Embedded Ag grid electrodes as current collector for ultraflexible transparent solid-state supercapacitor. ACS Appl. Mater. Interfaces 9, 27649-27656 (2017).
46. X. Rui, Y. Tang, O. I. Malyi, A. Gusak, Y. Zhang, Z. Niu, H.T. Tan, C. Persson, X. Chen, Z. Chen, Q. Yan, Ambient dissolution–recrystallization towards large-scale preparation of V2O5 nanobelts for high-energy battery applications. Nano Energy 22, 583-593 (2016).
47. C. X. Guo, K. Sun, J. Ouyang, X. Lu, Layered V2O5/PEDOT nanowires and ultrathin nanobelts fabricated with a silk reelinglike process. Chem. Mater. 27, 5813-5819 (2015).
48. W. Avansi Jr, C. Ribeiro, E.R. Leite, V.R. Mastelaro, Vanadium Pentoxide Nanostructures: An Effective Control of Morphology and Crystal Structure in Hydrothermal Conditions. Cryst. Growth Des. 9, 3626-3631 (2009).
49. C. Xiong, A.E. Aliev, B. Gnade and K.J. Balkus Jr. Fabrication of Silver Vanadium Oxide and V2O5 Nanowires for Electrochromics. ACS Nano 2, 293-301 (2008).
50. E. H. Lee, M. B. Lewis, P. J. Blau, L. K. Mansur, Improved surface properties of polymer materials by multiple ion beam treatment. J. Mater. Res. 6, 610-628 (1991).

51. B.H. Kim, W. G. Hong, H. R. Moon, S. M. Lee, J. M. Kim, S. Kang, Y. Jun, H. J. Kimet, Investigation on the existence of optimum interlayer distance for H2 uptake using pillared-graphene oxide. Int. J. Hydrogen Energy 37, 14217-14222 (2012).
52. Y. Zhou, Q. Bao, L.A.L. Tang, Y. Zhong, K.P. Loh, Hydrothermal Dehydration for the "Green" Reduction of Exfoliated Graphene Oxide to Graphene and Demonstration of Tunable Optical Limiting Properties. Chem. Mater. 21, 2950-2956 (2009).
53. D. R. Dreyer, S. Park, C.W. Bielawski, R. S. Ruoff, The chemistry of graphene oxide. Chem. Soc. Rev. 39, 228-240 (2010).
54. R. Baddour-Hadjean, V. Golabkan, J. Pereira-Ramos, A. Mantoux, D. Lincot, A Raman study of the lithium insertion process in vanadium pentoxide thin films deposited by atomic layer deposition. J. Raman Spectrosc. 33, 631-638 (2002).
55. A. Schaarschmidt, A.A. Farah, A. Aby, A.S. Helmy, Influence of nonadiabatic annealing on the morphology and molecular structure of PEDOT−PSS films. J. Phys. Chem. B 113, 9352-9355 (2009).
56. Z. Liu, K. Parvez, R. Li, R. Dong, X. Feng, K. Müllen, Transparent conductive electrodes from graphene/PEDOT:PSS hybrid inks for ultrathin organic photodetectors. Adv. Mater. 27, 669-675 (2015).
57. S. Kiruthika, C. Sow, G.U. Kulkarni, Transparent and flexible supercapacitors with networked electrodes. Small 13, 1701906:1-1701906:9 (2017).
58. J. J. Yoo, K. Balakrishnan, J. Huang, V. Meunier, B. G. Sumpter, A. Srivastava, M. Conway, A. L. M. Reddy, J. Yu, R. Vajtai, P.M. Ajayan, Ultrathin planar graphene supercapacitors. Nano Lett. 11, 1423-1427 (2011).
59. D. Li, W. Zhou, Q. Zhou, G. Ye, T. Wang, J. Wu, Y. Chang, J. Xu, Transparent 1T-MoS2 nanofilm robustly anchored on substrate by layer-by-layer self-assembly and its ultra-high cycling stability as supercapacitors. Nanotechnology 28, 395401:1-395401:7 (2017).
60. X. Y. Liu, Y.Q. Gao, G.W. Yang, A flexible, transparent, and super-long-life supercapacitor based on ultrafine Co3O4 nanocrystal electrodes. Nanoscale 8, 4227-4235 (2016).
61. Y. Wang, W. Zhou, Q. Kang, J. Chen, Y. Li, X. Feng, D. Wang, Y. Ma, W. Huang, Patterning islandlike MnO2 arrays by breath-figure templates for flexible transparent supercapacitors. ACS Appl. Mater. Interfaces 10, 27001-27008 (2018).
62. S. Bellani, L. Najafi, G. Tullii, A. Ansaldo, R. O.-Nuñez, M. Prato, M. Colombo, M. R. Antognazza, F. Bonaccorso, ITO nanoparticles break optical transparency/high-areal capacitance trade-off for advanced aqueous supercapacitors. J. Mater. Chem. A 5, 25177-25186 (2017).
63. E. Conway, Electrochemical Supercapacitors: Scientific Fundamentals and Technological Applications, Kluwer Academic/Plenum: New York, USA (1999).
64. A. J. Bard, M.V. Mirkin (Eds.) Scanning Electrochemical Microscopy; Marcel Dekker: New York, NY, USA (2001).
65. E. Laviron, General expression of the linear potential sweep voltammogram in the case of diffusionless electrochemical systems. J. Electroanal. Chem. 101, 19-28 (1979).
66. D. Fraggedakis, M. McEldrew, R. B. Smith, Y. Krishnan, Y. Zhang, P. Bai, William C. Chueh, Y. S-. Horn, M. Z. Bazantet, Theory of coupled ion-electron transfer kinetics. Electroch. Acta, 367, 137432:1-137432:17 (2021).
67. L. Wang, H. Yang, X. Liu, R. Zeng, M. Li, Y. Huang, X. Hu, Constructing hierarchical tectorum-like α-Fe2O3/PPy nanoarrays on carbon cloth for solid-state asymmetric supercapacitors. Angew. Chem. Int. Ed. 56, 1105-1110 (2017).
68. H. Gerischer, in Physical Chemistry: An Advanced Treatise; H. Eyring, D. Henderson, W. Jost (Eds.) Academic Press Inc. Vol. 9A, New York (1970).
69. L. M. Torres, A. F. Gil, L. Galicia, I. González, Understanding the Difference between Inner- and Outer-Sphere Mechanisms: An Electrochemical Experiment. J. Chem. Educ. 73, 808-810 (1996).
70. S. Gupta, B. Evans, A. Henson, S. B. Carrizosa, Salt-Assisted Ultrasonicated De-Aggregation and Advanced Redox Electrochemistry of Detonation Nanodiamond. Materials 10, 1292:1-1292:19 (2017) and references therein.